

Automated non-mass enhancing lesion detection and segmentation in breast DCE-MRI

Ignacio Alvarez Illan¹, Javier Ramirez¹, J.M. Gorriz¹, Katja Pinker², and Anke Meyer-Baese³

¹Signal Theory and Communications Department, Universidad de Granada, Spain

²Department of Radiology, Memorial Sloan-Kettering Cancer Center, New York, USA

³Scientific Computer Department, Florida State University, Tallahassee, FL 32306 USA

April 16, 2019

Abstract

Non-mass enhancing lesions (NME) constitute a diagnostic challenge in dynamic contrast enhanced magnetic resonance imaging (DCE-MRI) of the breast. Computer Aided Diagnosis (CAD) systems provide physicians with advanced tools for analysis, assessment and evaluation that have a significant impact on the diagnostic performance. Here, we propose a new approach for the specific problem of NME detection and segmentation, by taking advantage of independent component analysis (ICA) to extract a data-driven dynamic characterization of tissue. A set of independent sources was obtained from a dataset of patients, and the dynamic behavior of the different tissues was described by multiple dynamic curves, together with a set of eigenimages describing the scores for each voxel. A new test image is projected onto the independent source space using the unmixing matrix, and each voxel is classified by a support vector machine (SVM) that has already been trained with manually delineated data. A solution to the high false positive rate problem is proposed by controlling the SVM hyperplane location. The CAD system is trained and validated, reaching a DSC coefficient of 0.7215 for NME segmentation.

1 Introduction

Accurate methods for early diagnosis of breast cancer are important for determining prognosis and achieving favorable treatment. Following the introduction of dynamic-contrast-enhanced magnetic resonance imaging (DCE-MRI) research has demonstrated that enhancement kinetics on DCE-MRI has high diagnostic value for mass lesions [21]. However, non-mass-enhancing lesions (NME) exhibit a heterogeneous appearance with high variations in kinetic characteristics and morphological patterns on DCE-MRI [34]. Consequently, DCE-MRI has reported specificity and sensitivity of merely 35% and 73% for NME, much lower than that for mass-enhancing lesions. A set of computer aided diagnosis (CAD) systems for breast cancer diagnosis on DCE-MRI has been developed with satisfactory performance results. However, in the case of challenging lesions such as NME, the low specificity of such methods is unsatisfactory.

For a CAD system to be used in breast DCE-MRI two features are important to evaluate: i) the ability of the CAD to correctly differentiate between malignant and benign lesions; and

ii) the ability of the CAD system to correctly locate malignant lesions within the 3D spatial volume. To evaluate the first feature, the accuracy, specificity and sensitivity are usually reported. To evaluate the second feature, commonly the Dice similarity coefficient (DCS) is calculated between the CAD segmentation and some other ground truth segmentation. In most cases, a manual segmentation of the lesions is performed by experienced radiologists as ground truth. Two issues are well known in DCE-MRI for breast cancer diagnosis. The first is that, even for experienced radiologists, DCE-MRI is limited in specificity resulting in unnecessary breast biopsies [16]. Moreover, visual readings are prone to subjective errors [30]. The second issue is that CAD systems for breast cancer diagnosis have reported a high false positive rate, and consequently low specificity. However, this does not necessarily mean that CAD systems misclassify benign lesions as malignant. Therefore, it is not clear whether CAD systems can be optimized to improve lesion segmentation independently from lesion classification, or if regardless they will inherently suffer from the same limitations such as the low specificity reported in visual readings of DCE-MRI.

In this work we examined the relationship between the false positive rate of CAD systems for breast cancer diagnosis and lesion segmentation on DCE-MRI. To achieve our aim, we obtained rich characterization of data through advanced processing techniques, combined with machine learning paradigms intended for big data analysis and used the resulting information to build a CAD system. We did not introduce any *a priori* knowledge about the disease in the workflow in order that all information may be completely datadriven, which thereby also enabled us to identify new features not currently in the Breast Imaging Reporting and Data System (BI-RADS) classification criteria that could potentially improve segmentation of visual readings. Both morphological and dynamic features are considered in BI-RADs. However, in NME lesions, morphological characteristics are hard to define, making dynamic behavior the most important source of information. Therefore, using only dynamic information of the tissue, we performed a supervised method to detect and segment non-mass enhanced lesions on the breast.

Lesion segmentation has been successfully achieved using unsupervised clustering methods, [28], fuzzy c-means (FCM) [8] or improvements over FCM [22]. In unsupervised clustering, sophisticated pre-processing must be implemented to control the false positive rate, with fine tuning of parameters and/or heuristic steps. On the other hand, it has been demonstrated that processing of dynamic signals provides relevant information for classification of tissues, such as principal component analysis (PCA)-based decompositions closely related to the 3TP method [12].

Thus, we undertook a combination of supervised segmentation and signal processing to successfully segment NME lesions with control of the false positive rate. Independent component analysis (ICA) was used to extract a set of independent curves that described the possible dynamic behavior of different breast tissues. ICA has been shown to provide richer descriptions of underlying patterns than PCA [19, 20], and therefore was used for supervised classification in our work. We also incorporated machine learning, whereby we trained a classifier using the information encoded in a whole dataset of subjects, including the dynamic behavior of benign and malignant tissues. Considering features at the voxel level, the system 'learned' to characterize malignant tissues with a support vector machine (SVM). A procedure was implemented to fix the SVM hyperplane location, reducing and controlling the false positive rate. Projecting new unseen data using the unmixing matrix allowed us to obtain the features for estimating the generalization capabilities in a cross validation scheme, and compare it with visual readings of the images reported in the literature and other CAD system

approaches.

The methods proposed within this work demonstrate that NME can be detected with dynamic information by using multiple enhancement curves, providing a promising approach for improving breast cancer diagnosis. Accurate diagnostic methods as the one we hereby present may have an impact not only in accurate diagnosis, but also in reducing unnecessary breast biopsies.

1.1 Related work

The use of CAD systems to improve visual readings of DCE-MRI in breast cancer ranges from purely visual methods, to automatic classification. The present work combines visual comparison aspects with automatic classification techniques, thus adding value to purely visual comparison techniques based on PCA or Self-Organizing Map (SOM), such as in [12, 36], and complementing pure classification approaches, such as in [14, 7]. Specifically, the PCA approach of [12] extends the three point technique (3PT) by adding an eigenvector decomposition of the time signals. However, that decomposition does not provide an independent set of sources, but only a set of uncorrelated ones. The time-intensity curve estimation of [27] also seeks for hidden kinetics, but applies them to mass lesions. Concerning the automatic classification CADs, most approaches are concentrated on the detection and classification of mass enhancing lesions, by combining kinetic and morphological features [17, 14, 7, 37], like shape, margins, and internal enhancement distribution [1], textural kinetic [2], or more recently using deep neural networks [32, 3], among others. The detection and segmentation of lesions are usually performed as a manual or semi-manual task, in which regions of interest (ROIs) are manually defined or obtained from seeds with manual inputs.

For automatic lesion segmentation, keeping an acceptable false positive rate is a common issue in DCE-MRI CAD systems of the breast [25]. In many cases of these cases, unsupervised methods for lesion segmentation, such as FCM algorithms in [8, 6], are used and then the features extracted from the lesions are used for classification. Complex workflows that include vessel detection, whole breast segmentation, and several preprocessing steps have been proposed to control false positive detection [10, 18, 28, 22].

2 Methods

2.1 ICA-based enhancement curve analysis

Each voxel of the DCE-MRI image has a time signal representing the enhancement dynamics of different breast tissues. A set of DCE-MRI time signals can be analyzed in terms of the blind source separation problem, which proposes that the different dynamic behavior can be expressed as a linear combination of a reduced set of sources, making very little assumptions on the nature of that combination. ICA offers a solution to the blind source separation problem estimating a set of sources that maximizes the statistical independence between them, measured in terms of a cost function. In the literature, several functions have been used to measure statistical independence between signals [9]. Here, we used the fastICA algorithm [29] with mutual information as measure function (see appendix for details). Contrary to other eigenimage decompositions based on spatial-ICA, like in face recognition [4] and brain imaging [19, 24], the independent sources are obtained here in the temporal domain or, in other words, we work on a voxel level.

Thus, each voxel defines a temporal curve $\mathbf{x}(t_n)$ with t_1, \dots, t_N temporal points. A set of voxels $\{\mathbf{x}_i\}, i = 1, \dots, M$, defines the $M \times N$ matrix \mathbf{X} of observed signals, and the task of ICA will be to find the mixing matrix \mathbf{A} and the set of *sources* \mathbf{S} :

$$\mathbf{X} = \mathbf{A}\mathbf{S} \quad (1)$$

The mixing matrix or scores matrix \mathbf{A} assigns p coefficients a_{qp} to each voxel location $q = 1, \dots, M$, whose values measured the importance of each source to recover that voxel dynamics, by linearly combining them (see figure 1). In the rest of the paper, we will refer to these coefficients as the *scores*.

It is important to stress that working on a voxel level will allow data from different patients to be included in the matrix set \mathbf{X} . Therefore, the obtained set of sources \mathbf{S} does not have to be restricted to represent the particular dynamic enhancement present in a single subject, but can be used to model all the possible curves that independently characterize each BI-RADs category.

For new unseen data $\tilde{\mathbf{x}}$, the scores are extracted from $\tilde{\mathbf{x}}$ by projecting it onto the subspace E spanned by the source signals from the matrix \mathbf{S} . Specifically, let $\{\mathbf{s}_1, \dots, \mathbf{s}_p\}$ be the basis set of independent sources spanning the subspace E , then \mathbf{S} denote the p -by- N matrix of which columns are $\mathbf{s}_1, \dots, \mathbf{s}_p$. Since this basis need not be orthogonal, a well known result of linear algebra stated that the projection is given by:

$$\mathbf{P}_S = \mathbf{S}(\mathbf{S}^T\mathbf{S})^{-1}\mathbf{S}^T \quad (2)$$

so that the application of that operator on a voxel signal $\tilde{\mathbf{x}}(t)$:

$$\mathbf{a} = \mathbf{P}_S\tilde{\mathbf{x}} \quad (3)$$

projects it to the subspace E , obtaining its p scores \mathbf{a} on that subspace. Contrary to other related methods, such as PCA, ICA does not provide a natural way to sort the p independent components. However, it is a relevant question whether or not a reduced set $l < p$ of components contain noisy and discardable information. The mean squared error (MSE) between the enhancement time signals and the reconstructed signals using the k source \mathbf{s}_k and its corresponding score \mathbf{a}_k , is calculated as:

$$MSE(k) = \frac{1}{N_t \cdot N_r} \sum_{i,j} (\mathbf{x}_i(t_j) - \mathbf{a}_k \cdot \mathbf{s}_k(t_j))^2 \quad (4)$$

and used as a parameter to measure the noise content of each \mathbf{s}_k source, with $k = 1, \dots, p$.

The independent component scores \mathbf{a}_k of the dataset is used as feature vectors inputs of a SVM to learn the different enhancement patterns associated with malignant and benign tissues.

2.2 False positive rate control by SVM hyperplane traslation

SVM is a machine learning algorithm that separates a given set of binary labeled training data with a hyperplane that is maximally distant from the two classes (known as the maximal margin hyper-plane). The objective is to build a function $f : \mathbb{R}^p \rightarrow \{1, 0\}$ using training data, consisting of p -dimensional patterns \mathbf{x}_i and class labels y_i :

$$(\mathbf{x}_1, y_1), (\mathbf{x}_2, y_2), \dots, (\mathbf{x}_M, y_M) \in (\mathbb{R}^p \times \{1, 0\}), \quad (5)$$

so that f will correctly classify new examples $(\tilde{\mathbf{x}}, y)$. The problem of finding the maximal margin hyperplane is usually solved by quadratic programming algorithms that try to minimize a margin cost function J :

$$J(\mathbf{w}, w_0, \xi) = \frac{1}{2} \|\mathbf{w}\|^2 + C \sum_{i=1}^l \xi_i, \quad (6)$$

subject to the inequality constraints:

$$y_i[\mathbf{w}^T x_i + w_0] \geq 1 - \xi_i, \quad \xi_i \geq 0 \quad i = 1, 2, \dots, l. \quad (7)$$

where the slack variables ξ_i incorporate to the optimization those feature vectors that are not separable (details can be found in [35]). The solution to that problem can be expressed by a linear combination of a subset of vectors, called support vectors:

$$d(\mathbf{x}) = \sum_{i=1}^{N_S} \alpha_i y_i K(\mathbf{s}_i, \mathbf{x}) + w_0 \quad (8)$$

where $K(., .)$ is the kernel function, α_i is a weight constant derived from the SVM process and \mathbf{s}_i are the N_S support vectors [35]. Taking the sign of the function leads to the binary classification solution.

Here, we propose a SVM hyperplane translation in terms of the slack variables ξ_i , to control the number of false positives. We add a new term $g(\mathbf{s}_i, \xi_i)$ to the hyperplane defining function $d(\mathbf{x})$, so that the classification solution is now defined by:

$$f(\mathbf{x}) = \text{sign}\{d(\mathbf{x}) + g(\mathbf{s}_i, \xi_i)\} \quad (9)$$

where the function g takes the two-class average distance to the hyperplane of those support vectors with $\xi_i > 1$, measured by the kernel metric K . Common kernels that are used by SVM practitioners for the nonlinear feature mapping are:

- Polynomial

$$K(\mathbf{x}, \mathbf{y}) = [\gamma(\mathbf{x} \cdot \mathbf{y}) + c]^d. \quad (10)$$

- Radial basis function (RBF)

$$K(\mathbf{x}, \mathbf{y}) = \exp(-\gamma \|\mathbf{x} - \mathbf{y}\|^2). \quad (11)$$

as well as the linear kernel, in which $K(., .)$ is simply a scalar product, and therefore g in equation 9 would average the euclidean distance in that particular case.

2.3 Dataset

We collected a set of data from 13 patients with NME. The data represented a patient subset from a larger cohort undergoing MRI following patient inclusion criteria described in detail in [31]. The imaging protocol comprised of both high spatial and temporal resolution MRI. High spatial resolution imaging was acquired with a 3T MRI scanner (Tim Trio, Siemens,

Erlangen, Germany) with a dedicated, bilateral, 4-channel breast coil in vivo (Orlando, FL). Three high spatial resolution images were taken, pre-contrast, peak, and postcontrast as coronal T1-weighted (3D) FLASH sequence, with water excitation and fat suppression, with the following sequence parameters: TR/TE 877/3.82 milliseconds; FOVr 320 mm, SI 1 mm isotropic, 96 slices, flip angle 9° , matrix 320 / 134, 1 average, acquisition time 2 minutes. Low-spatial high temporal resolution, contrast-enhanced, coronal T1-weighted (VIBE) sequence was obtained with the following sequence parameters: TR/TE 3.61/1.4 milliseconds, FOVr 320 mm, SI 1.7 mm isotropic, 72 slices, flip angle 6° , matrix 192 / 192, 1 average, 13.2 seconds acquisition time per volume leading to 3.45 minutes for 17 measurements. A second set of high spatial resolution T1-weighted imaging (repeated 3D-FLASH) was acquired after these 17 low spatial VIBE resolution images, as the peak enhancement of the lesion could be expected at the end of this time span([31] and references therein). Finally, high temporal resolution (repeated VIBE with 25 measurements, leading to an acquisition time of 5 minutes 35 seconds and repeated 3D-FLASH for dynamic assessment of lesion wash-out) was performed, and then high spatial resolution T1-weighted images were recorded. The contrast agent used was Gd-DOTA (generic name: Gadoterate meglumine; Dotarem, Guerbet, France), injected intravenously as a bolus (0.1 mmol per kilogram body weight) and administered with a power injector (Spectris Solaris EP, Medrad, Pittsburgh, PA) at 4 mL/s followed by a 20 mL saline flush. The contrast agent was injected 75 seconds after starting the first coronal T1-weighted VIBE.

The NME were visually assessed by expert radiologists following the American College of Radiology BI-RADS atlas [33], and delineated using the Osirix software on the 3T high spatial resolution volumes. All NME were classified as BI-RADS 4: suspicious or BI-RADS 5: highly suspicious of malignancy. The lesions found were histopathologically confirmed, from which 5 were invasive ductal carcinoma (IDC), 5 ductal carcinoma in-situ (DCIS) and 3 invasive lobular carcinoma (ILC).

2.4 Preprocessing

All dynamic sequences were registered to the pre-contrast volume. This pre-processing step was required to remove any spatial misalignments on the sequence caused by involuntary movements of the patient. The algorithm employed to perform this task was the SPM12 [13] registration algorithm, which performs affine and non-affine transformations on the data by minimizing a similarity measure cost function, selected to be the mutual information metric. Afterwards, a 3D gaussian filter of size 2FWHM was used to smooth the images.

The manual delineations of the lesions were performed on 3T high-spatial resolution images using the Osirix software, recorded as a set of axial point coordinates. The besenham algorithm [5] was used to transform the coordinate points into 3D binary masks, and a decimation was employed to downsample the masks to the size of the low spatial high-temporal resolution images. Thus, the downsampled masks were used to define the class labels of each voxel, 1 if the voxel was in the mask, and 0 otherwise.

2.5 Evaluation

The dataset was divided into three subsets: training data, validation data and testing. The training and validation data were obtained from a set of 3 DCE-MRI images containing 6 delineated lesions, five DCIS and one IDC, all which had BIRADS grades of 2-3, and were

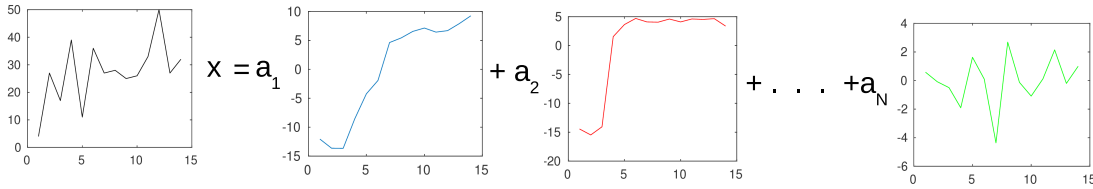


Figure 1: Decomposition of a sample time signal \mathbf{x} into a linear combination of independent sources and its corresponding scores $\mathbf{a}_1, \mathbf{a}_2, \dots, \mathbf{a}_N$.

histopathologically confirmed. The data were considered at the voxel level, first removing the voxels that lie inside the thoracic cavity and the chest wall as well as background voxels. In spite of the existence of automatic and accurate methods for performing whole breast segmentation [11, 15, 23, 38], we performed this task straightforwardly finding the middle chest point as in [7], and discarding the content of the image after this point, reducing the original number of $192 \times 192 \times 72 \approx 2.6 \cdot 10^6$ voxels contained in each image to $\approx 1.6 \cdot 10^5$, and guaranteeing the exclusion of heart and other organs noisy-signals. Without any loss of generality, the exclusion of some healthy breast tissue from the training set was necessary for a balanced training of the SVM, since the malignant voxel samples would be outnumbered by the benign ones by several orders of magnitude. Therefore, after discarding non-relevant parts of the image, a random selection of $N_a \approx 5 \cdot 10^3$ benign voxel samples from the pool of all non-lesion voxels of the images was performed to balance the training set, resulting on a $2 * N_a \times p$ training and validating data matrix.

The voxel data were used as in input to the fastICA algorithm, obtaining a set of scores for each voxel that served as feature vectors for training and validating a SVM in a cross validation scheme. The validation step is preformed in two stages:

- First, different parameters were optimized within a 10-fold cross-validation scheme: i)

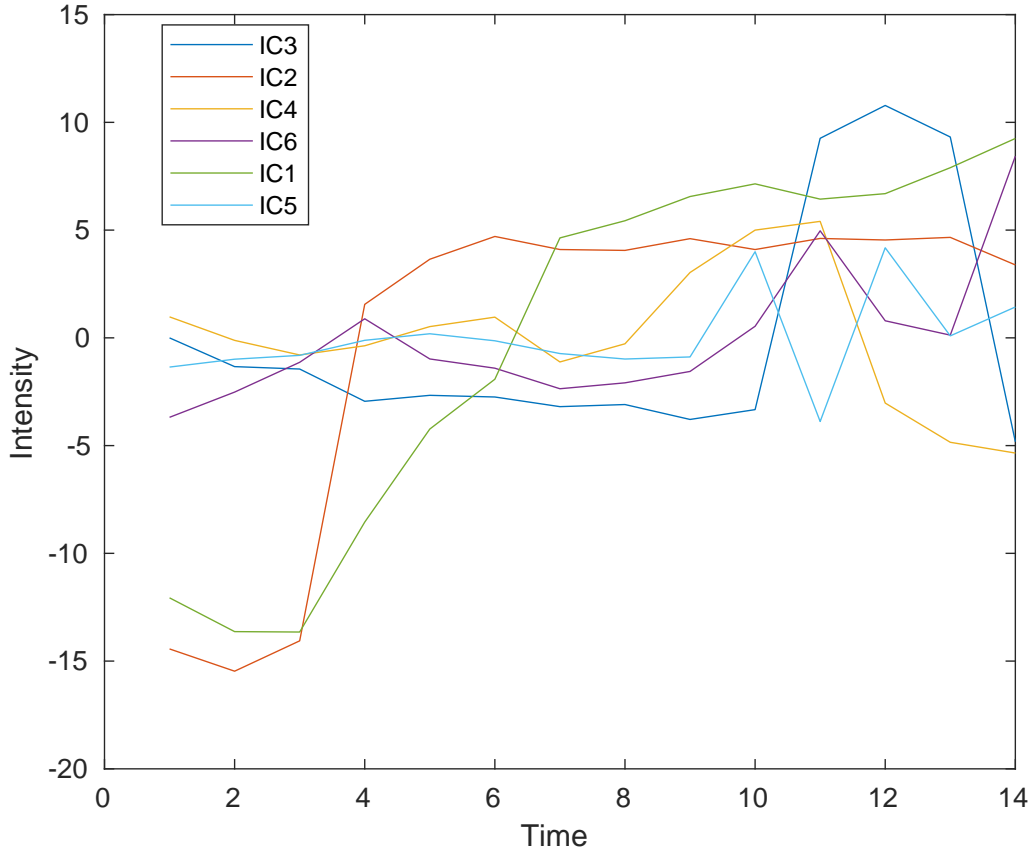


Figure 2: First six independent components sorted by MSE. In red, the IC2 shows typical 'malignant' dynamics, while in green, IC1 shows a persistent enhancement curve, characteristic of benign tissues.

the optimal dimensionality of the data h ; ii) the optimal kernel (linear, polynomial or RFB). The optimal value for h was obtained by sorting the independent components by their MSE defined in equation 4, and the feature space dimension was changed by sequentially increasing the number of components included on the scores. The optimal kernel was selected by comparing the classification performance, based on the classification error.

- Secondly, once the number of components and the kernel function were fixed, the decision boundary location of the SVM was analysed in an enlarged test dataset of size $\approx 4 \cdot 10^5$, that contained all the discarded voxels in the validation step.

3 Results

The scores defined in equation (1) are depicted in two different spaces: the 3D DCE-MRI space coregistered with the original data (figure 3), and the E subspace spanned by the two first independent components s_1 and s_2 (figure 7), sorted according to the MSE defined criteria.

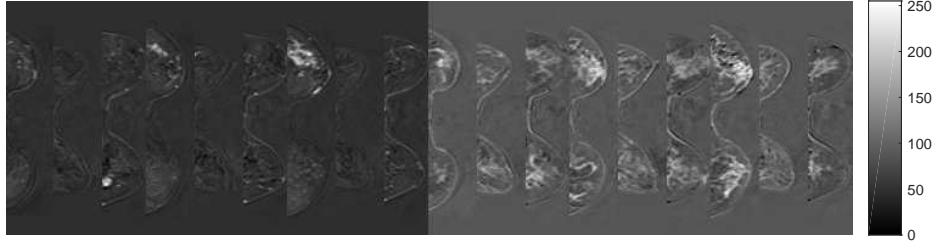


Figure 3: Three representative axial slices from three training patients. Intensity represents voxelwise scores of the first and second independent component in the 3D MRI space. The scores of the second IC, on the left, correspond with the IC in red in figure 2). The scores of the first IC, on the right, correspond with the IC in green in figure 2)

The representation in the 3D DCE-MRI space shows that similar score values are grouped together around tissues that have a similar enhancement. On the left, voxels belonging to the lesions present a high score value, revealing that the associated independent component encodes the malignant dynamic information. On the right, the distribution of score values does not concentrate in specific regions, but spreads over the breast tissues revealing a relation with normal tissue enhancement dynamics. That information complements the representation on the E subspace, where a clear separation between tumor tissues represented in blue, and normal tissues in red, can be inferred, although some region of overlapping is present. Also, the independent components \mathbf{s}_1 and \mathbf{s}_2 are shown in figure 2, together with other extracted sources. It is interesting to note that, being automatically data-driven extracted, these independent components take the form of enhancement curves: curve IC1 is a normal enhancement, while curve IC2 has a 'typical' malignant behavior, according to model based descriptions [21]. The remaining set of independent components cannot be assigned to any particular dynamic, nor tend to form clusters of similar enhancement when depicted in 3D, therefore not possessing an obvious interpretation. However, the common classification onto wash-out, plateau and permanent enhancement of dynamic curves is reduced by ICA to only two clearly identifiable curves. Therefore, the ICA based signal processing analysis reveals that dynamic enhancement curves reaching a plateau do not behave independently in the ICA sense from washout curves, while permanent enhancement curves do.

The results of the 10-fold cross-validation are shown in figures 7 and 4, and also in the left part of table 1. In figure 7, the $2 * N_a \times p$ training data are shown after the SVM is trained,

and the obtained support vectors are marked with circles. In figure 4, the loss is displayed for different SVM kernels and increasing number of ordered components by the MSE score defined in equation 4 for ICA, and increasing variance for PCA. The loss function used to obtain the values is the hinge loss function:

$$L(y, f(\mathbf{x})) = \max(1 - yf, 0) \quad (12)$$

This loss function penalizes the wrongly classified samples, while the correctly ones do not contribute. Therefore, higher L values are related to a high false positive rate within the training set. PCA performance with both kernels indicates a bigger overlap than ICA between features in different classes within the training set. The best performance results are obtained with ICA using a linear kernel, with a loss rate around 0.12 that does not strongly depend on the number of components used. However, a decreasing error rate is achieved by increasing the number of independent components used. A similar performance is obtained using a RBF kernel when the dimensionality of the feature space h is below 3. When the number of components is increased above this value, the loss rate grows until it reaches values comparable to PCA performance. This discrepancy between the behavior of both kernels for ICA and SVM suggests that increasing the complexity of the model increases the risk of overfitting, requiring additional adjustments that impact on the performance. From figure 4, it is also possible to confirm that the ordering criteria proposed in 4 does in fact sort the independent components in a meaningful manner: the last value is obtained when all the independent components are used, thus fixing a *maximum possible value* in the loss rate. If a value below the that maximum is found, it can be understood as a improvement in the feature selection. Since it is the case for number of components below 3, it can be argued that, at least for the very first cases, the sorting criteria is selecting the most representative components.

Table 1: Performance parameters on training and validating data

| | Training | | | | Validation DSC | | |
|------------------|------------|----------|-------------|-------------|----------------|------------------|--|
| | Hinge Loss | Accuracy | Specificity | Sensitivity | d=0 | max | DSC(μ_d) [DSC($\mu_d \pm \sigma_d$)] |
| PCA + linear SVM | 0.9764 | 0.7263 | 0.6581 | 0.7944 | 0.61±0.02 | 0.6765±0.0005 | 0.6620 [0.6074-0.4339] |
| PCA + RBF SVM | 0.9529 | 0.7263 | 0.6581 | 0.7944 | 0.61±0.02 | 0.6765±0.0005 | 0.6620 [0.6074-0.4339] |
| ICA + linear SVM | 0.1254 | 0.9501 | 0.9410 | 0.9593 | 0.35±0.01 | 0.73±0.01 | 0.7215 [0.5633-0.6164] |
| ICA + RBF SVM | 0.1083 | 0.9515 | 0.9573 | 0.9457 | 0.29±0.01 | 0.44±0.04 | 0.1085 [0.3711-0.0559] |
| raw + linear SVM | 2.4429 | 0.8026 | 0.8446 | 0.7605 | 0.30±0.13 | 0.6±0.1 | 0.4650 [0.2735-0.6112] |

Figure 5 shows the NME delineated by the expert radiologist (in red), together with a distance-to-hyperplane map (distance $d = 0$ is represented by a black contour). The value of each voxel in the map is defined in equation 8. It can be seen that hyperplane location (value $d = 0$) produces big regions of false positives. Those regions are mostly concentrated around the delimited lesion, but extended regions can also be found in non-connected regions where benign dynamics are expected. The false positive rate can be controlled by modifying the defining value of the hyperplane location, set to 0 by definition in SVM. Translating the hyperplane towards the positive values produces a more conservative definition of feature vectors belonging to the +1 class. Therefore, only score values high above the hyperplane would be considered as malignant, while intermediate values not clearly projecting malignant-related score values will not be classified as lesion, decreasing the false positive rate and increasing specificity. However, there must be a compromise between specificity and sensitivity, since increasing the defining value of the decision function also has an impact on the false negative

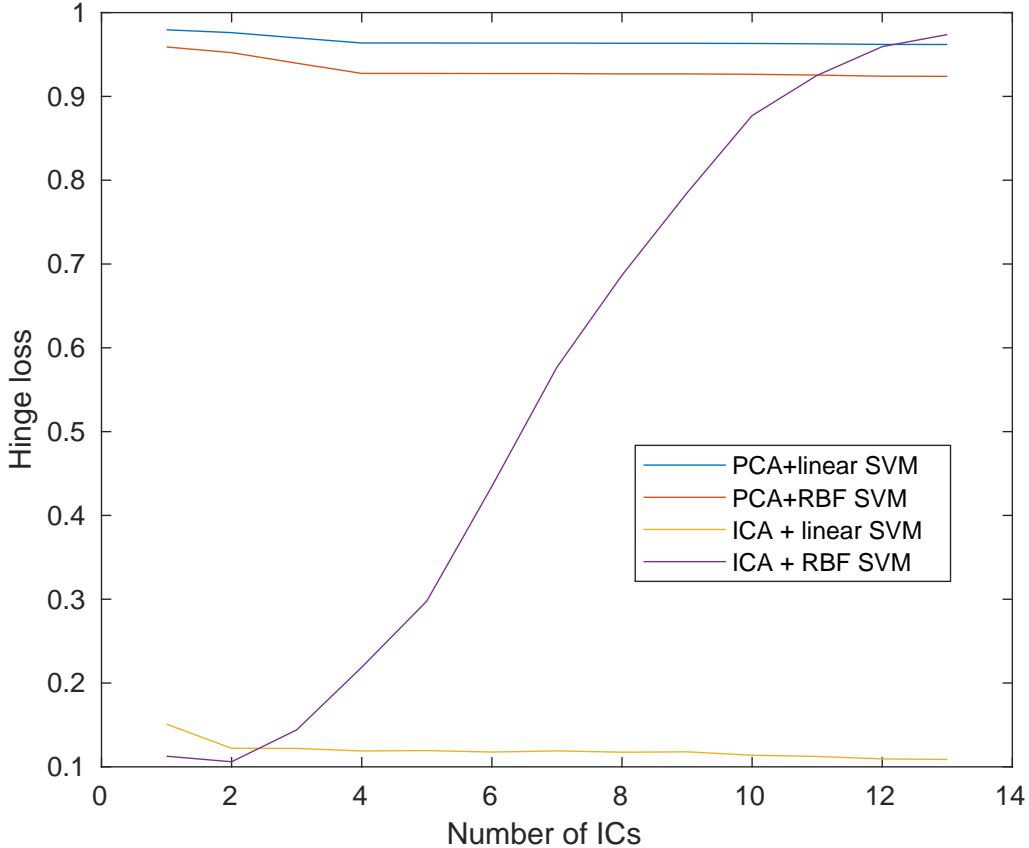


Figure 4: Hinge loss on the 10-fold cross-validation scheme for linear kernel and RFB kernel by varying the number of components on PCA and ICA. ICA components are sorted according to MSE.

rate. This trade-off requires to be very finely tuned, as there exists a big disequilibrium between the number of +1 class samples and the number of -1 class samples. The several-orders of magnitude bigger number of benign samples produce an imbalance in the validation of the SVM classifier. In figure 8, the influence of the imbalanced classes can be perceived if compared with the scatter plot of the scores considering only the reduced training data of figure 7. Although other solutions exist to the problem of imbalanced dataset in SVM classification, we propose here a very conservative approach, in which the hyperplane defining value is translated into the +1 class region, guaranteeing that only very distant scores from the hyperplane are considered as malignant. The value into which the hyperplane is rotated $DSC(\mu_d)$ is defined in equation 9. Other values could be used to make this transformation, but are prone to be affected by outlier support vectors that uncontrollably increase the false negative rate. By averaging the support vector's distance to the hyperplane with the condition $\xi_i > 1$, we are smoothing the effect of possible outlier support vectors, while translating the hyperplane to actual relevant values. Alternatively, we calculate the decision defining value experimentally, in the second validation on the training data, and test both on the test set: the theoretically derived value and the experimentally adjusted one. In the special case

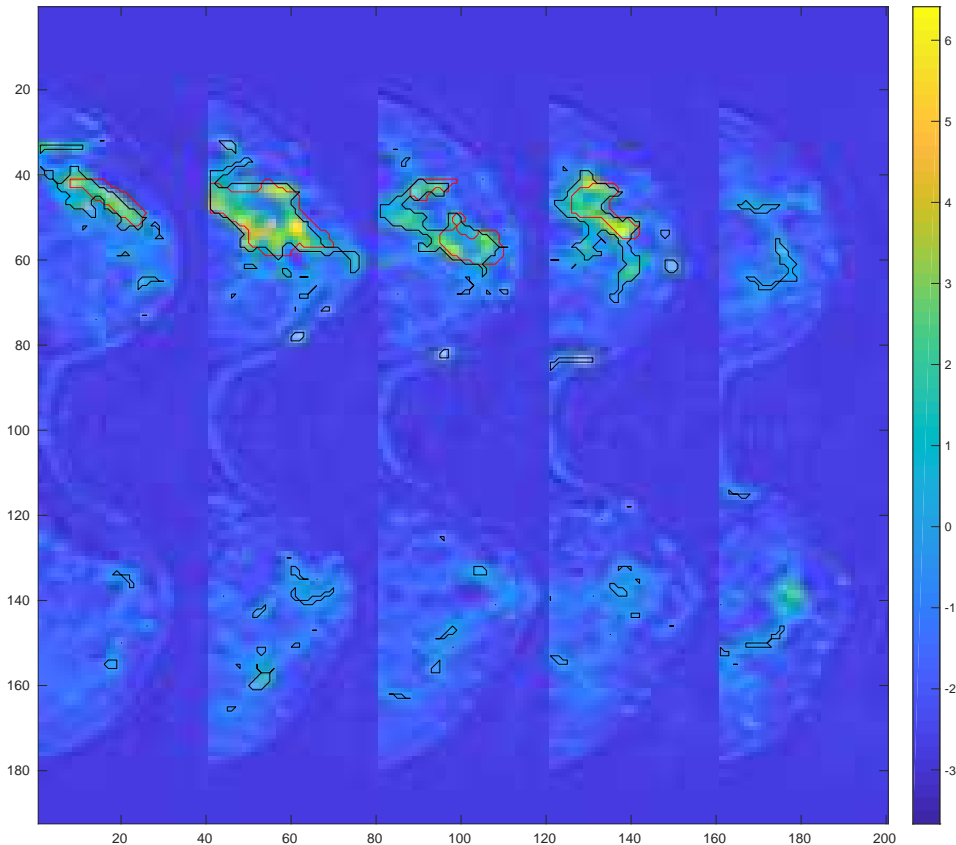


Figure 5: Five representative axial slices of a NME. The values on voxels represent the distance to the hyperplane after classification on a trained SVM. The black contour represents the location of the hyperplane and the red contour is the manual delineation of the lesion.

in which all ξ_i are less than 1, we average the support vector's distance to the hyperplane with the condition $1 > \xi_i > 0$.

To evaluate the lesion detection performance, the DSC is calculated, defined as:

$$DSC = 2 * \frac{A \cap M}{A \cup M} \quad (13)$$

and measures the amount of overlap between segmentation algorithms (A) and manually-generated (M) segmentations with respect to the size of the segmented region.

Table 1 shows the validation values obtained by default SVM at $d = 0$, at empirical maximum, and at proposed value, for 2 component PCA, ICA and raw data using 2 kernels. Raw data is displayed for reference, and corresponds to the use of dynamic curves as feature vectors for SVM, without multicurve extraction. PCA method [12] shows higher DSC at $d = 0$ than the proposed ICA approach. Hyperplane translation has a lower effect in the PCA case since all support vectors lie in the $\xi_i < 1$. In the ICA with a linear kernel case,

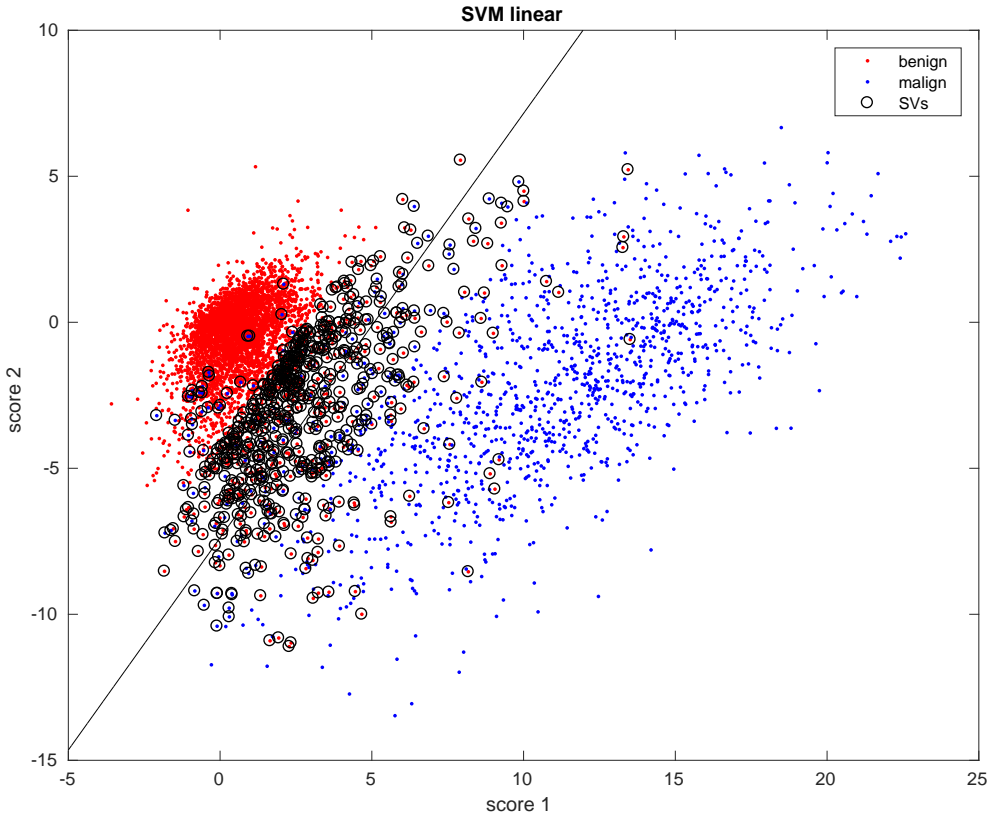


Figure 6: DSC for the validation data obtained by varying the decision defining value of the SVM hyperplane.

the false positives are reduced significantly reaching the maximum DSC values, in agreement with the interval of maximum empirical values.

Figure 6 shows the DCS coefficients obtained by applying the false positive control defined previously to the most relevant case of ICA processing using 2 independent components and a linear kernel. The validation results (in blue) are shown together with the DSC at mean distance μ_d of the $\xi_i > 1$ support vectors (red), and its corresponding standard deviation interval (green). The DSC coefficient reaches a maximum by shifting the SVM hyperplane location approximately to $d = -2$. Although not displayed, the outlier support vectors defining the margin are at a maximum distance of $d = -4$, where the DSC is less than in $d = 0$. Therefore, locating the hyperplane at the mean distance μ_d duplicates the DSC, and prevents the effect of outliers. Moreover, the proposed value $DSC(\mu_d)$ is achieved within the margins of the actual empirical maximum, proving that the controlling strategy improves the DSC coefficient, reaching a peak value of 0.7215.

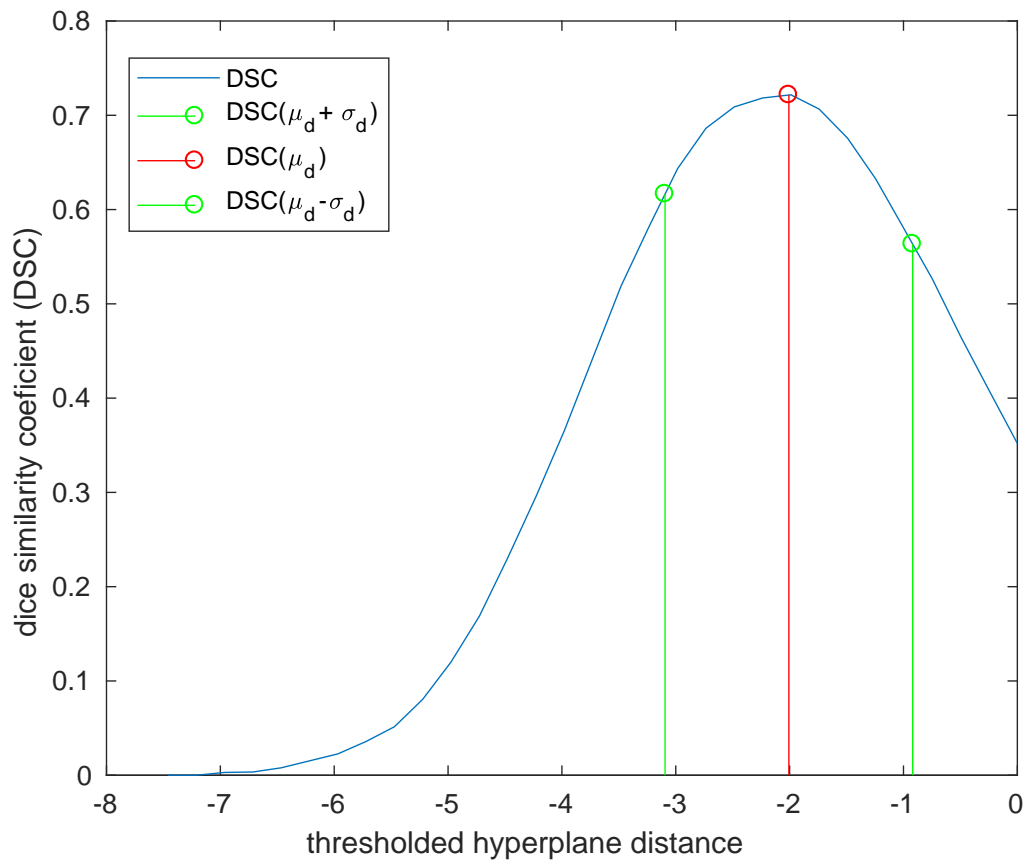


Figure 7: Scatter plot of the scores corresponding to the two first independent components of the training data, together with the linear decision SVM function (in black) and the support vectors (SVs).

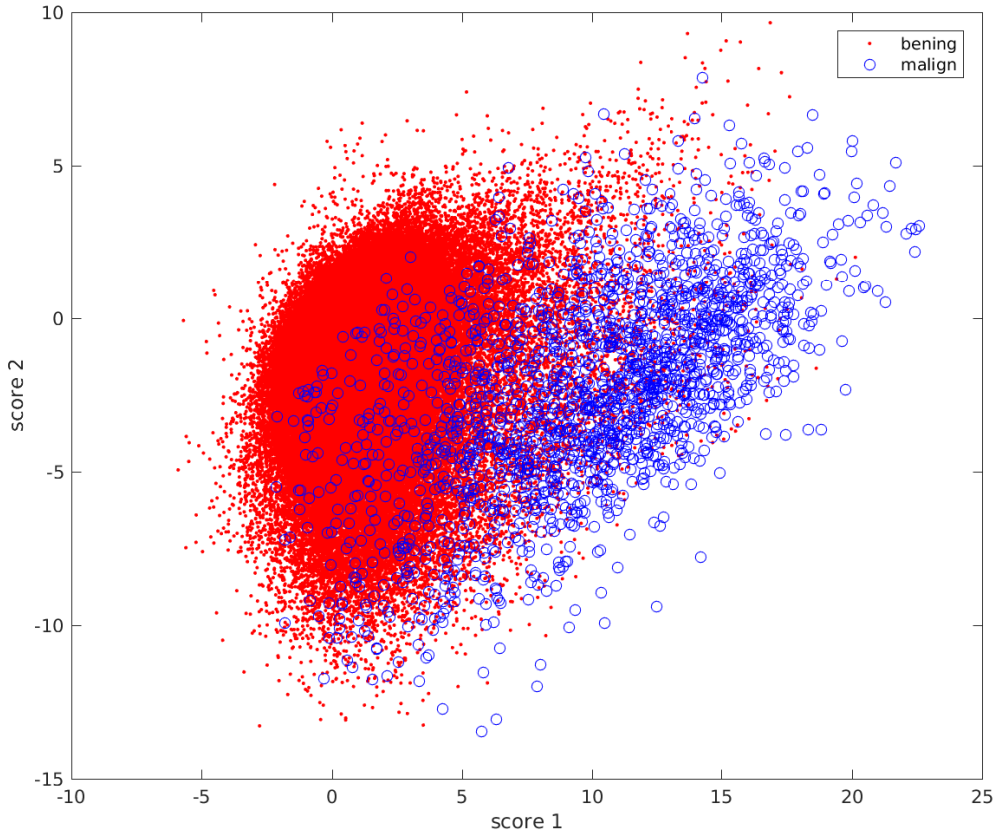


Figure 8: Scatter plot of the scores corresponding to the two first independent components of the validation data.

4 Discussion

The contributions of this work are two-fold: First, visual interpretations of DCE-MRI image can be enriched by using the proposed ICA-based processing of time signals, which produces a data-driven decomposition of dynamic enhancement signals into a multi-curve description, that are statistically independent and disease specific. The idea of producing multiple-curves to characterize lesions has also been explored by Lui et. al. [27], but from the total variation perspective, which is not data-driven but based on assumptions on the data. Other visual methods based on CAD techniques, as PCA in Eyal et. al. [12] or PCA-SOM-LDD in Varini [36] have been proposed in the literature, to enrich the well-known 3TP method. Thus, visual support is an important characteristic to evaluate in aiding diagnosis of breast cancer by computer systems. The presented approach outperforms PCA based methods as shown in table 1 in terms of automatic segmentation performance, and provides a meaningful visual support for experienced and unexperienced readers.

The validation and comparison of our results would be ideally tested in an open-source database, publicly available to researchers who are developing DCE-MRI CAD systems for

breast cancer, since differences in acquisition, patient characteristics and spatio-temporal MRI resolution, among others, may have an impact on the comparison of CAD performance parameters. Moreover, the low incidence of NME lesions reduces the available testing data, therefore limiting the validation of the presented method.

The second contribution is the *supervised* nature of the detection and segmentation method, which allows control of the false positive rate. Most CAD systems for lesion classification start from a manual or semi-manual ROI delimitation [12, 7, 37], that limits control of the false positives. The baseline approach to lesion segmentation is the FCM unsupervised method, which in Liang et. al. [26] is reported to have a $6\% \pm 9\%$ of overlap with manually defined regions, and is commonly used in many CAD systems for breast cancer diagnosis in DCE-MRI. In Jayender et. al. [22], an enhancing pre-processing step is added to the usual FCM algorithm using linear dynamic system modeling. The overlap of the algorithm output with the radiologists' segmentation and CADstream output, computed in terms of DSC, was 0.77 and 0.72 respectively. In the unsupervised approach of Cui et al [10], a combination of Gaussian mixture modeling and a marker-controlled watershed transform was used to segment the lesions. The overall overlap ratio between the two radiologists' manual segmentations and the proposed algorithm was $64.3\% \pm 10.4\%$. The supervised method of Liang et. al. [26] shows overlap rates with the ground truth of $51\% \pm 26\%$ and $48\% \pm 25\%$. This method required a robust intensity normalization method to make intra-patient comparisons, while the ICA-method presented here characterizes the form of the curve, thus not requiring intensity normalization. Moreover, we report higher or comparable DSC values that those in the literature, even in the more challenging case of NME.

5 Conclusions

This paper presents promising results for challenging NME breast lesion detection in DCE-MRI. We present an approach that develops a linear expansion of features for every voxel in the image based on ICA, allowing for a *multicurve* characterization of the enhancement behavior, in contrast with usual single-curve voxel characterization. The data-driven obtained features are used to train and test an SVM with satisfactory performance. In addition, previously the imbalanced nature of the interest class features limited automatic detection by supervised methods as SVM. In this work, we propose parameter optimization on the SVM hyperplane location, such that the false positive rate is controlled, thus providing a solution to the low specificity problem in CAD of breast cancer. With that optimization the DSC value is increased approximately a 50% from the default $d = 0$ margin value, reaching a peak value of 0.7215.

6 Acknowledgments

This work has received funding from the European Unions Horizon 2020 research and innovation programme under the Marie Skłodowska-Curie grant agreement No 656886. Katja Pinker also received support from the NIH/NCI Cancer Center Support Grant P30 CA008748.

References

- [1] S. Agliozzo, M. De Luca, C. Bracco, A. Vignati, V. Giannini, L. Martincich, L. A. Carbonaro, A. Bert, F. Sardanelli, and D. Regge. Computer-aided diagnosis for dynamic contrast-enhanced breast MRI of mass-like lesions using a multiparametric model combining a selection of morphological, kinetic, and spatiotemporal features. *Medical Physics*, 39(4):1704–1715, 2012.
- [2] S. C. Agner, S. Soman, E. Libfeld, M. McDonald, K. Thomas, S. Englander, M. A. Rosen, D. Chin, J. Noshier, and A. Madabhushi. Textural kinetics: a novel dynamic contrast-enhanced (DCE)-MRI feature for breast lesion classification. *Journal of Digital Imaging*, 24(3):446–463, 2011.
- [3] N. Antropova, B. Huynh, and M. Giger. SU-D-207b-06: Predicting Breast Cancer Malignancy On DCE-MRI Data Using Pre-Trained Convolutional Neural Networks. *Medical Physics*, 43(6Part4):3349–3350, June 2016.
- [4] M. Bartlett, J. Movellan, and T. Sejnowski. Face recognition by independent component analysis. *IEEE Transactions on Neural Networks*, 13(6):1450–1464, 2002.
- [5] J. E. Bresenham. Algorithm for computer control of a digital plotter. *IBM Systems Journal*, 4(1):25–30, 1965.
- [6] Y.-C. Chang, Y.-H. Huang, C.-S. Huang, P.-K. Chang, J.-H. Chen, and R.-F. Chang. Classification of breast mass lesions using model-based analysis of the characteristic kinetic curve derived from fuzzy c-means clustering. *Magnetic Resonance Imaging*, 30(3):312–322, Apr. 2012.
- [7] Y.-C. Chang, Y.-H. Huang, C.-S. Huang, J.-H. Chen, and R.-F. Chang. Computerized breast lesions detection using kinetic and morphologic analysis for dynamic contrast-enhanced MRI. *Magnetic Resonance Imaging*, 32(5):514–522, 2014.
- [8] W. Chen, M. L. Giger, and U. Bick. A fuzzy c-means (FCM)-based approach for computerized segmentation of breast lesions in dynamic contrast-enhanced MR images. *Academic Radiology*, 13(1):63–72, Jan. 2006.
- [9] P. Comon. Independent component analysis, a new concept? *Signal Process.*, 36(3):287–314, 1994.
- [10] Y. Cui, Y. Tan, B. Zhao, L. Liberman, R. Parbhu, J. Kaplan, M. Theodoulou, C. Hudis, and L. H. Schwartz. Malignant lesion segmentation in contrast-enhanced breast MR images based on the marker-controlled watershed. *Medical Physics*, 36(10):4359–4369, Oct. 2009.
- [11] M. U. Dalm, G. Litjens, K. Holland, A. Setio, R. Mann, N. Karssemeijer, and A. Gubern-Mrida. Using deep learning to segment breast and fibroglandular tissue in MRI volumes. *Medical Physics*, 44(2):533–546, Feb. 2017.
- [12] E. Eyal, D. Badikhi, E. Furman-Haran, F. Kelcz, K. J. Kirshenbaum, and H. Degani. Principal component analysis of breast DCE-MRI adjusted with a model-based method. *Journal of magnetic resonance imaging: JMRI*, 30(5):989–998, Nov. 2009.

- [13] K. Friston, J. Ashburner, S. Kiebel, T. Nichols, and W. Penny. *Statistical Parametric Mapping: The Analysis of Functional Brain Images*. Academic Press, 2007.
- [14] A. Gubern-Merida, R. Marti, J. Melendez, J. L. Hautth, R. M. Mann, N. Karssemeijer, and B. Platel. Automated localization of breast cancer in DCE-MRI. *Medical Image Analysis*, 20(1):265–274, 2015.
- [15] A. Gubern-Mrida, L. Wang, M. Kallenberg, R. Mart, H. K. Hahn, and N. Karssemeijer. Breast segmentation in MRI: quantitative evaluation of three methods. In *Medical Imaging 2013: Image Processing*, volume 8669, page 86693G. International Society for Optics and Photonics, Mar. 2013.
- [16] S. H. Heywang-Kbrunner, P. Viehweg, A. Heinig, and C. Kchler. Contrast-enhanced MRI of the breast: accuracy, value, controversies, solutions. *European Journal of Radiology*, 24(2):94–108, Feb. 1997.
- [17] S. Hoffmann, J. D. Shutler, M. Lobbes, B. Burgeth, and A. Meyer-Bse. Automated analysis of non-mass-enhancing lesions in breast MRI based on morphological, kinetic, and spatio-temporal moments and joint segmentation-motion compensation technique. *EURASIP Journal on Advances in Signal Processing*, 2013(1):172, 2013.
- [18] L. Hu, Z. Cheng, M. Wang, and Z. Song. Image manifold revealing for breast lesion segmentation in DCE-MRI. *Bio-Medical Materials and Engineering*, 26(s1):S1353–S1360, Jan. 2015.
- [19] I. A. Illan, J. M. Gorriz, J. Ramirez, D. Salas-Gonzalez, M. M. Lopez, F. Segovia, R. Chaves, M. Gomez-Rio, and C. G. Puntonet. 18f-FDG PET imaging analysis for computer aided alzheimers diagnosis. *Information Sciences*, 181(4):903–916, 2011.
- [20] J. Illan, I. A. Gorriz, J. Ramirez, D. Salas-Gonzalez, M. Lopez, F. Segovia, P. Padilla, and C. Puntonet. Projecting independent components of SPECT images for computer aided diagnosis of alzheimer’s disease. *Pattern Recognition Letters*, 31(11):1342–1347, 2010.
- [21] S. A. Jansen, A. Shimauchi, L. Zak, X. Fan, G. S. Karczmar, and G. M. Newstead. The diverse pathology and kinetics of mass, nonmass and focus enhancement on MR imaging of the breast. *Journal of magnetic resonance imaging : JMRI*, 33(6):1382–1389, June 2011.
- [22] J. Jayender, S. Chikarmane, F. A. Jolesz, and E. Gombos. Automatic Segmentation of Invasive Breast Carcinomas from DCE-MRI using Time Series Analysis. *Journal of magnetic resonance imaging : JMRI*, 40(2):467–475, Aug. 2014.
- [23] L. Jiang, X. Hu, Q. Xiao, Y. Gu, and Q. Li. Fully automated segmentation of whole breast using dynamic programming in dynamic contrast enhanced MR images. *Medical Physics*, 44(6):2400–2414, June 2017.
- [24] L. Khedher, I. A. Illn, J. M. Grriz, J. Ramrez, A. Brahim, and A. Meyer-Baese. Independent Component Analysis-Support Vector Machine-Based Computer-Aided Diagnosis System for Alzheimers with Visual Support. *International Journal of Neural Systems*, 27(03):1650050, July 2016.

- [25] J. E. D. Levman, C. Gallego-Ortiz, E. Warner, P. Causer, and A. L. Martel. A Metric for Reducing False Positives in the Computer-Aided Detection of Breast Cancer from Dynamic Contrast-Enhanced Magnetic Resonance Imaging Based Screening Examinations of High-Risk Women. *Journal of Digital Imaging*, 29(1):126–133, Feb. 2016.
- [26] X. Liang, K. Ramamohanara, H. Frazer, and Q. Yang. Lesion Segmentation in Dynamic Contrast Enhanced MRI of Breast. In *2012 International Conference on Digital Image Computing Techniques and Applications (DICTA)*, pages 1–8, Dec. 2012.
- [27] H. Liu, Y. Zheng, D. Liang, P. Tang, F. Ren, L. Zhang, and Z. Zhao. Total variation based DCE-MRI decomposition by separating lesion from background for time-intensity curve estimation. *Medical Physics*, n/a–n/a, 2017.
- [28] D. McClymont, A. Mehnert, A. Trakic, D. Kennedy, and S. Crozier. Fully automatic lesion segmentation in breast MRI using mean-shift and graph-cuts on a region adjacency graph. *Journal of Magnetic Resonance Imaging*, 39(4):795–804, Apr. 2014.
- [29] E. Oja. A fast fixed-point algorithm for independent component analysis. *Neural Computation*, 9:1483–1492, 1997.
- [30] E. B. Pages, I. Millet, D. Hoa, F. C. Doyon, and P. Taourel. Undiagnosed Breast Cancer at MR Imaging: Analysis of Causes. *Radiology*, 264(1):40–50, July 2012.
- [31] K. Pinker, G. Grabner, W. Bogner, S. Gruber, P. Szomolanyi, S. Trattinig, G. Heinz-Peer, M. Weber, F. Fitzal, U. Pluschnig, M. Rudas, and T. Helbich. A combined high temporal and high spatial resolution 3 tesla MR imaging protocol for the assessment of breast lesions: Initial results. *Investigative Radiology*, 44(9):553–558, 2009.
- [32] R. Rasti, M. Teshnehlab, and S. L. Phung. Breast cancer diagnosis in DCE-MRI using mixture ensemble of convolutional neural networks. *Pattern Recognition*, 72:381–390, Dec. 2017.
- [33] V. A. C. o. R. Reston. *Breast Imaging Reporting and Data System Atlas BI-RADS-MRI*. American College of Radiology, 2003.
- [34] N. Sakamoto, M. Tozaki, K. Higa, Y. Tsunoda, T. Ogawa, S. Abe, S. Ozaki, M. Sakamoto, T. Tsuruhara, N. Kawano, T. Suzuki, N. Yamashiro, and E. Fukuma. Categorization of non-mass-like breast lesions detected by MRI. *Breast Cancer*, 15(3):241–246, July 2008.
- [35] V. N. Vapnik. *Statistical Learning Theory*. John Wiley and Sons, Inc., New York, 1998.
- [36] C. Varini, A. Degenhard, and T. W. Nattkemper. Visual exploratory analysis of DCE-MRI data in breast cancer by dimensional data reduction: A comparative study. *Biomedical Signal Processing and Control*, 1(1):56–63, Jan. 2006.
- [37] T.-C. Wang, Y.-H. Huang, C.-S. Huang, J.-H. Chen, G.-Y. Huang, Y.-C. Chang, and R.-F. Chang. Computer-aided diagnosis of breast DCE-MRI using pharmacokinetic model and 3-D morphology analysis. *Magnetic Resonance Imaging*, 32(3):197–205, Apr. 2014.
- [38] S. Wu, S. P. Weinstein, E. F. Conant, M. D. Schnall, and D. Kontos. Automated chest wall line detection for whole-breast segmentation in sagittal breast MR images. *Medical Physics*, 40(4), Apr. 2013.